Quantifying the response of a synthetic light curve generation model to varying inputs.

Laurence D. J. Blacketer[1], **Prof. Hugh G. Lewis**[1], and **Dr. Hodei Urrutxua**[2]

[1] *Astronautics Research Group, The University of Southampton, Southampton SO17 1BJ, UK*
[2] *Universidad Rey Juan Carlos, Calle Tulipán, s/n, 28933 Móstoles, Madrid, Spain*

August 28, 2018

Abstract

Ensuring that operating within the near-Earth space environment does not become hampered by increasing numbers of Resident Space Objects (RSOs) is an important focus for the global space industry. Following research indicating a self-sustaining population of RSOs between 900 - 1000 km driven by collision activity, Active Debris Removal (ADR), the targeted removal of a RSO, was proposed as a possible reactive countermeasure. All of the most viable ADR proposals require accurate characterisation of the target object's motion both for target selection and for the removal manoeuvre.

Another way of safeguarding near-Earth space is through improving upon current Space Situational Awareness (SSA) capabilities. Through better and more accurate positioning, a level of traffic control can be applied to space environment. This would allow for unwanted events to be identified in advance, and responded to more proactively.

In either case, new techniques need to be developed for deriving information on object motion, from observation data. The attitude state of the object is of particular interest to both SSA and ADR. For SSA, the attitude of the object has a significant effect on the drag force, which is by far the largest force exerted on objects in Low Earth Orbit (LEO). As for ADR, the majority of proposals require a physical interface with the target object and as a result will rely heavily on attitude state characterisation.

Of the available techniques for remote observation and measurement of space objects, optical measurements are by far the cheapest and simplest. As a result, large quantities of time-varying brightness data, on a range of active, inactive and unknown objects, has been collected. Hence developing techniques to derive information, such as attitude state, from light curves could be highly beneficial to ADR and SSA efforts.

To examine the availability of attitude information in optical light curve data, a Synthetic Light Curve Forward Model (SLCFM) has been developed. The model uses positional data acquired from the Two Line Element (TLE) database and the Jet Propulsion Laboratory (JPL) HORIZONS database. Brightness is simulated through application of a Cook-Torrence Bidirectional Distribution Reflectance Function (BDRF) to a faceted object geometry. The model inputs are therefore an object geometry, attitude state and the BDRF parameters that define the reflection properties of the surface.

This paper quantifies the response of the SLCFM to changes in the inputs by measuring a distance in Hilbert space, using the Chebyshev basis. The synthetic light curves were found to be sensitive to attitude state. It was also found that incorrectly modelling the object geometry and surface optical characteristics can result in significant differences in the resultant light curve.

1 Introduction

With the large numbers of Resident Space Objects (RSOs) within the near-Earth space environment, the development of Space Situational Awareness (SSA) techniques and technologies have become a focus throughout the global space sector. One objective of an SSA program is to minimise the risk of operation in space through improving positioning

and tracking capabilities. An additional application is in the implementation of a space traffic management system. The aim of such a system would be to exert some level of traffic control over the near-Earth space environment in order to further reduce the possibility of unwanted interactions between RSOs.

A further point of consideration is Active Debris Removal (ADR), the targeted removal of an RSO. ADR has been presented as a possible solution to a predicted collision-activity-driven growth in the number of debris fragments between 900 and 1000 kilometres, even in the absence of future launch activity [8], [9]. First identified by debris modelling carried out by the National Aeronautics and Space Administration (NASA), it was subsequently observed using other debris modelling tools, such as the University of Southampton's Debris Analysis and Monitoring Architecture for the Geosynchronous Environment (DAMAGE) [7]. Although the uncertainties in long term future debris modelling are high, removing objects from space may be a valuable tool for ensuring the sustainability of the near-Earth space environment, and so research and technology demonstration missions are ongoing in this area. One of the most crucial phases of an ADR mission is interfacing with the object. A number of solutions are being researched including robotic arms, harpoons and nets. In any case, accurate attitude determination will be required for selection of suitable targets, and also for carrying out the mission itself. Other fields, such as on-orbit servicing and research into attitude-dependent effects such as drag and solar radiation pressure, could also benefit from these techniques.

The largest force experienced by objects in near-Earth orbits is atmospheric drag, which is highly dependent on the object orientation. With a known attitude state this force could be modelled much more accurately, potentially improving predictions of the object's future position. Attitude state could therefore be highly beneficial for SSA applications. However, because the vast majority of RSOs are uncooperative, the attitude determination must rely on observation data alone.

A range of sensors are employed for measurements of space objects. Although highly powerful radar and optical installations are capable of generating accurate measurements, their low number and high cost preclude them from more general application to the RSO population. Alternatively large numbers of small, automated, optical telescopes have been deployed across the globe. One example is the Mini-MegaTORTORA (MMT) system operated by Kazan Federal University, which maintains a publicly accessible catalogue of light curve data, available at `astroguard.ru/satellites` [1]. As a result, large volumes of optical light curves, which have heritage in attitude and shape detection of Near-Earth Objects (NEOs) such as asteroids [3], [10], [5], have been collected on a wide range of different space objects. Hence optical light curves could potentially form an integral component of a future SSA infrastructure.

To explore the attitude detection capability of optical light curves, a synthetic light curve forward model (SLCFM) has been developed. Previous research has examined forward modelling of light curve data and found the results to be highly dependent on the accuracy of the light curve model [12]. The observability of attitude in a single light curve has been examined analytically using the Fisher information matrix. These results found small attitude perturbations to be undetectable in a single light curve. However it is proposed that modelling the object dynamics across a series of measurements could increase the attitude observability [4]. On this basis, and to form a foundation for future work into attitude determination, this paper quantifies the response of the SLCFM to the various inputs and identifies the key sensitivities.

2 Methodology

The SLCFM was developed with an objective of simulating real light curve data. This generated a requirement for ephemerides of the Sun, Earth and the object. The NASA Jet Propulsion Laboratory (JPL) HORIZONS database provides the celestial positions and the object position is acquired using Two Line Element (TLE) data together with the Simple General Perturbations 4 (SGP4) propagator.

The synthetic light curve is generated through application of a Bidirectional Distribution Reflectance Function (BDRF) to a faceted geometry of the object. The Cook-Torrence model was selected in order to handle the specular component of reflection. This has been shown to be useful for deriving information on attitude state, such as rotation period and

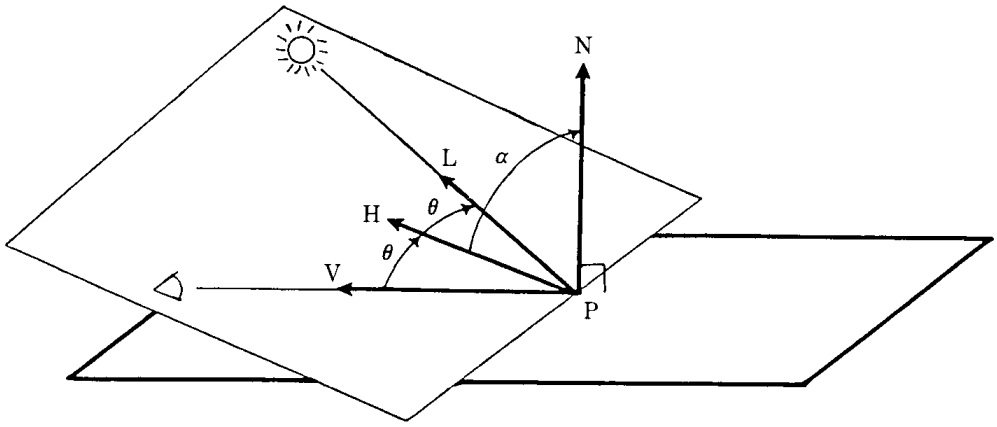

Figure 1: *Illumination Geometry [2].*

rotation axis [2], [6].

Fig. 1 shows the reflection geometry and labels the illumination vector, $\boldsymbol{L}$, the observation vector $\boldsymbol{V}$, the angular bisector of these two vectors, $\boldsymbol{H}$ and the two angles α and θ. Representing some shape using a faceted geometry allows the apparent magnitude of a collection of N_{facets} facets to be given by the sum:

$$m = -26.74 - 2.5\ log_{10}\left(\sum_{i=1}^{N_{facets}} \frac{B_i}{4\pi r^2}\right) \tag{1}$$

where -26.74 is the apparent magnitude of the Sun, B_i is the ratio of incident to reflected flux at the i^{th} facet, and r is the distance between the surface and the observer. The Cook-Torrence BDRF is then used to calculate a value for B_i, using the equation:

$$B_i = (sR_s + dR_d)\pi A_i(\boldsymbol{N}_i \cdot \boldsymbol{L})(\boldsymbol{N}_i \cdot \boldsymbol{V}) \tag{2}$$

where R_s and R_d are the specular and diffuse bidirectional reflectances, A_i is the i^{th} facet area, and s and d are the specular and diffuse coefficients, where $s + d = 1$. The two bidirectional reflectances are given by:

$$R_d = \frac{\omega}{\pi} \tag{3}$$

where ω is the diffuse albedo of the surface, and:

$$R_s = \frac{F}{\pi}\frac{DG}{(\boldsymbol{N} \cdot \boldsymbol{L})(\boldsymbol{N} \cdot \boldsymbol{V})} \tag{4}$$

where F is the Fresnel term, G is the geometric attenuation factor and D is the facet slope function. The geometric attenuation factor is calculated from:

$$G = min\left\{1,\ \frac{2(\boldsymbol{N} \cdot \boldsymbol{H})(\boldsymbol{N} \cdot \boldsymbol{V})}{(\boldsymbol{V} \cdot \boldsymbol{H})}, \frac{2(\boldsymbol{N} \cdot \boldsymbol{H})(\boldsymbol{N} \cdot \boldsymbol{L})}{(\boldsymbol{V} \cdot \boldsymbol{H})}\right\} \tag{5}$$

using the angular bisector, H, calculated from:

$$H = \frac{\boldsymbol{V} + \boldsymbol{L}}{length(\boldsymbol{V} + \boldsymbol{L})} \tag{6}$$

The facet slope function is calculated using the Beckmann distribution:

$$D = \frac{1}{m^2 \cos^4(\alpha)} \exp^{-[\tan(\alpha)/m]^2} \tag{7}$$

where m, is the Root Mean Square (RMS) slope defining surface roughness and α is the angle between the angular bisector and the facet normal. Higher values for m indicate a rougher surface and therefore a wider distribution in the reflection. Finally the Fresnel equation is used to calculate the Fresnel term:

$$F = \frac{1}{2}\frac{(g-c)^2}{(g+c)^2}\left\{1 + \frac{[c(g+c)-1]^2}{[c(g-c)+1]^2}\right\} \tag{8}$$

where:

$$c = \cos(\theta) = \boldsymbol{V} \cdot \boldsymbol{H} \tag{9}$$

and

$$g^2 = n^2 + c^2 - 1 \tag{10}$$

Rearranging Schlick's approximation gives the index of refraction, n, as:

$$n = \frac{1+\sqrt{F_0}}{1-\sqrt{F_0}} \tag{11}$$

where for simplicity in this initial study, the reflectance at normal incidence, F_0, is taken as being equal to the diffuse albedo, ω [2], [12].

Application of this theory to each illuminated and observable facet, at each time point, allows for production of a synthetic light curve. Assuming that the illumination geometry is defined by a real light curve, the controllable BDRF inputs are the diffuse and specular coefficients s and d; the diffuse albedo ω and the RMS slope term m. Hence together with some discretised geometry and attitude state, the final synthetic light curve can be generated.

In order to quantify changes in the light curve, functional analysis and measure theory is used. From measure theory, the synthetic light curves are measurable, finite, square-integrable functions in the domain of the light curve. They are therefore contained within the L^2 Lebesgue Hilbert space, defined on this domain. A Hilbert space is a generalisation of Euclidean space into infinite-dimensions. As a result, analogous properties such as inner products and distances can be calculated between elements in the space. To parameterise a function in Hilbert space, some infinite subset of orthonormal basis functions is required. Subsequently all elements in the L^2 Hilbert space can be written as an infinite sum of these simple basis functions, as per the equation:

$$f(x) = \sum_{i=1}^{\infty} c_i T_i(x) \tag{12}$$

The Chebyshev basis functions were selected for being most appropriate for non-periodic signals and because they quickly converge. T_i and c_i are therefore the Chebyshev polynomials and Chebyshev coefficients of degree i. The L^2 norm of some function, f, in this space is defined as:

$$\|f\| = \left(\int_X |f|^2 \, d\mu\right)^{\frac{1}{2}} \tag{13}$$

Thus, the distance between two functions, f and g, in L^2 space is defined to be:

$$d(f,g) = \|f-g\| \tag{14}$$

The distance between two functions in Hilbert space is only zero when they are identical. This metric can therefore be used to quantify how different two functions are from one another [11].

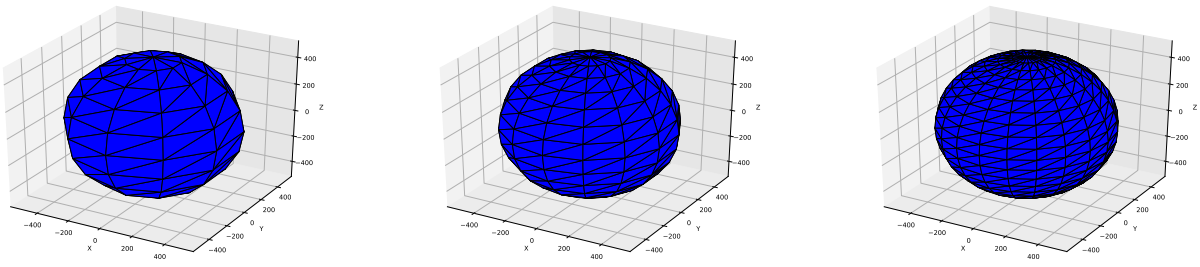

Figure 2: *Examples of three object geometries with increasing numbers of facets.*

Table 1: Table of model inputs.

Input Parameter	Value
Start Time	02:05:27 22/12/2016 UTC
Stop Time	02:09:58 22/12/2016 UTC
Duration	271 s
Observation Site Longitude	41.43 deg
Observation Site Latitude	41.43 deg
Observation Site Altitude	2030 m
Attitude	[0, 0, 0] $radians$
Attitude Motion	[0, 0, 0] $radians/s$
BDRF d	1.0
BDRF s	0.0

3 Results

The distance metric requires a base case from which to measure. The number of facets used in the object geometry is by far the largest cause of computational expense and so minimising this number can save a considerable amount of simulation time. Number of facets was therefore selected as the primary baseline. Eleven different geometry cases were examined. Each was an approximation of a sphere, using an incremental number of horizontal and vertical vertices from 10 - 20. Each geometry case therefore had an increasing number of facets from 180 - 760, whilst maintaining a 1 m diameter. A sphere was selected because there should be no attitude state dependence on perceived brightness. Examples of three of the geometries, in the satellite-centred inertial reference frame, are presented in Fig 2.

As the specular and diffuse components can be handled individually, the operation of the diffuse component will be examined first. The diffuse coefficient d, was set to 1.0 and a real light curve was used to define positions and reflection angles. The RMS slope term, m, contributes only to the specular reflection and so is ignored. Attitude and attitude motion were each set to zero. Table 1 presents this input data.

Fig. 3 shows the first result for varying the diffuse albedo term, ω, from 0.1 - 1.0. Each data point plots distance in Hilbert space from the 760 facet geometry base case. Trend lines, calculated through a least squares fitting to a power law function, have been added. On the left-hand graph, distance is measured from the $\omega = 1.0$ case, and the right-hand graph plots distance from the $\omega = 0.1$ case.

Next, the effect of initial attitude was examined. Using the same inputs as above but with a diffuse albedo set to $\omega = 0.5$, eleven equally spaced initial attitude cases from $0 - \pi$ radians were used. Fig. 4 contains four graphs showing the results of adding this attitude separately into each the x, y and z directions, in addition to equally into all three. Distance is measured from the zero attitude and attitude motion case. The graphs in Fig. 5 repeat this simulation, but for zero attitude and eleven equally spaced attitude motions between $0 - 1$ rotations per minute.

Now the operation of the specular component of the model is examined. For simplicity, the reflectance at normal

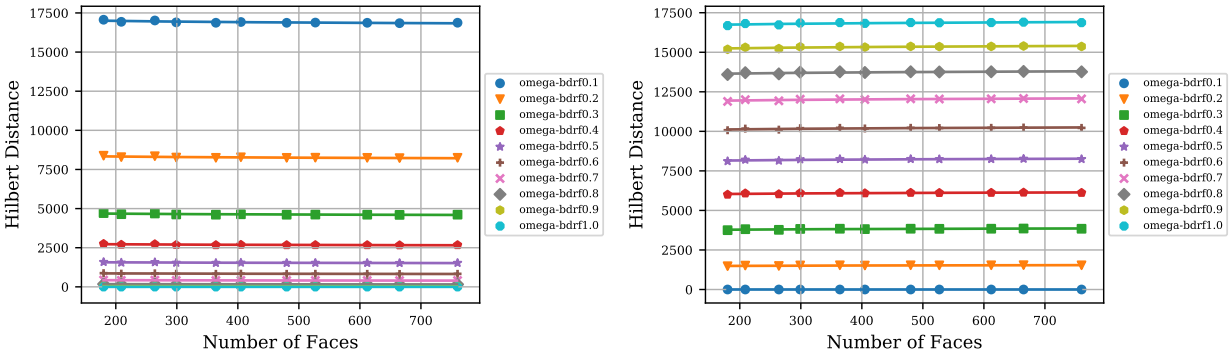

(a) Distance measured from the $\omega = 1.0$ case.

(b) Distance measured from the $\omega = 0.1$ case.

Figure 3: Plots of Hilbert distance against facet number for a diffuse albedo ranging from 0.1 - 1.0. Distance is measured from a 760-facet spherical geometry, with zero initial attitude and zero attitude motion.

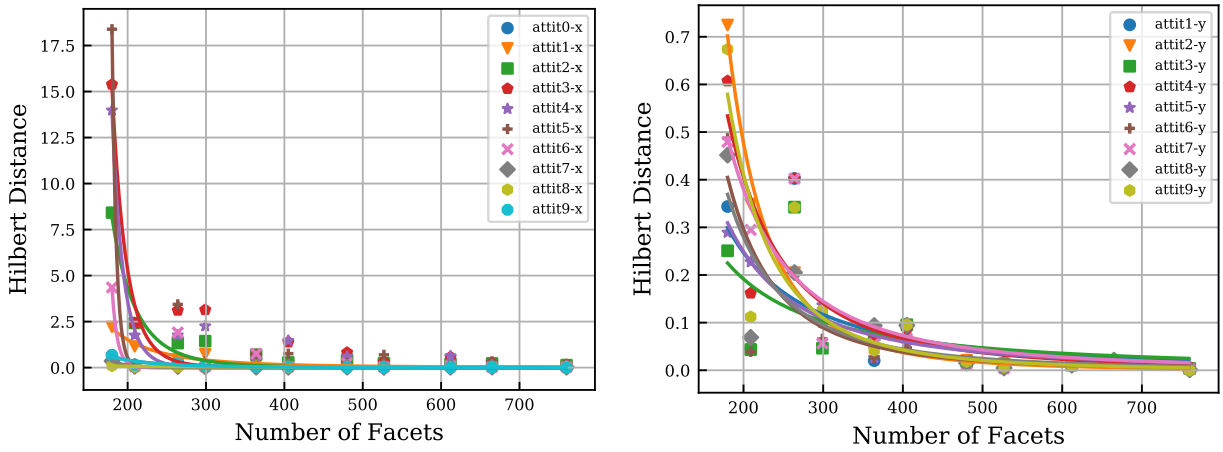

(a) Increasing initial x-attitude.

(b) Increasing initial y-attitude.

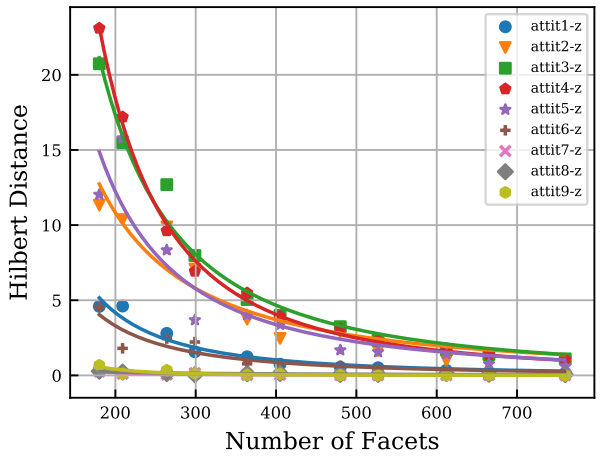

(c) Increasing initial z-attitude.

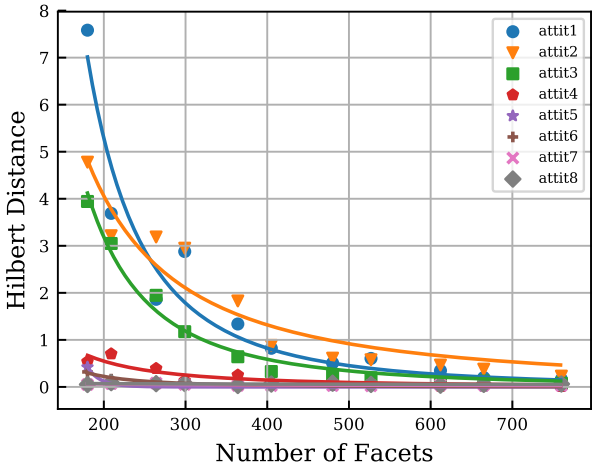

(d) Increasing initial attitude, equally into x, y and z.

Figure 4: Hilbert distance resulting from changes in initial attitude. Distance is measured from the 760-facet zero-attitude case and the reflection is purely diffuse.

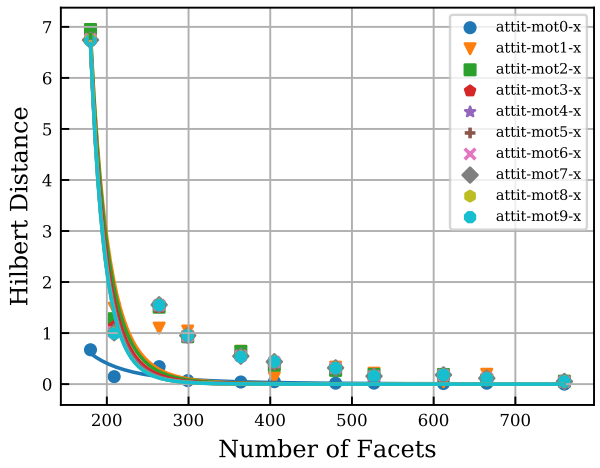

(a) Increasing x-attitude motion.

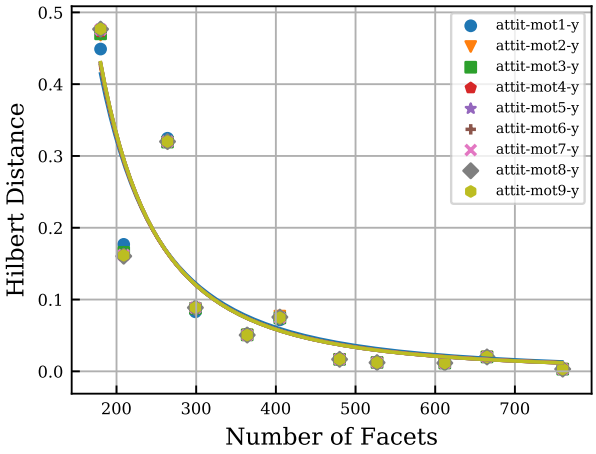

(b) Increasing y-attitude motion.

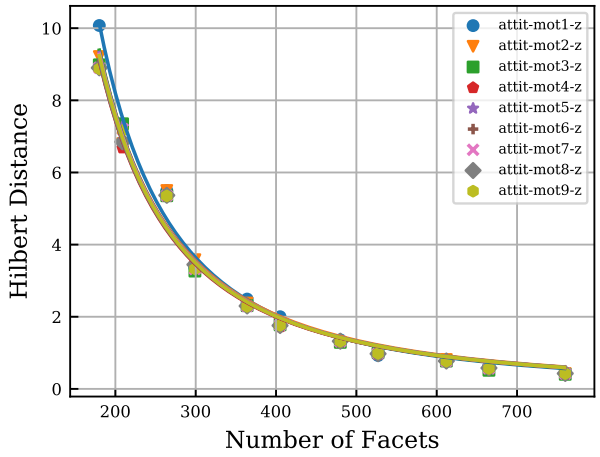

(c) Increasing z-attitude motion.

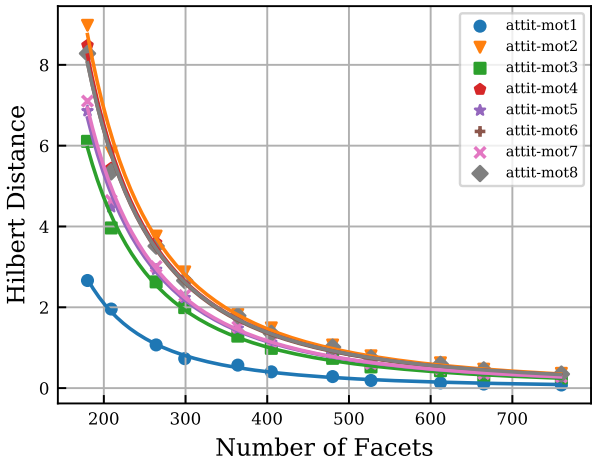

(d) Increasing attitude motion, equally into x, y and z.

Figure 5: Hilbert distance as a result of changes in attitude motion. Distance is measured from a 760-facet zero-attitude case for a purely diffuse reflection.

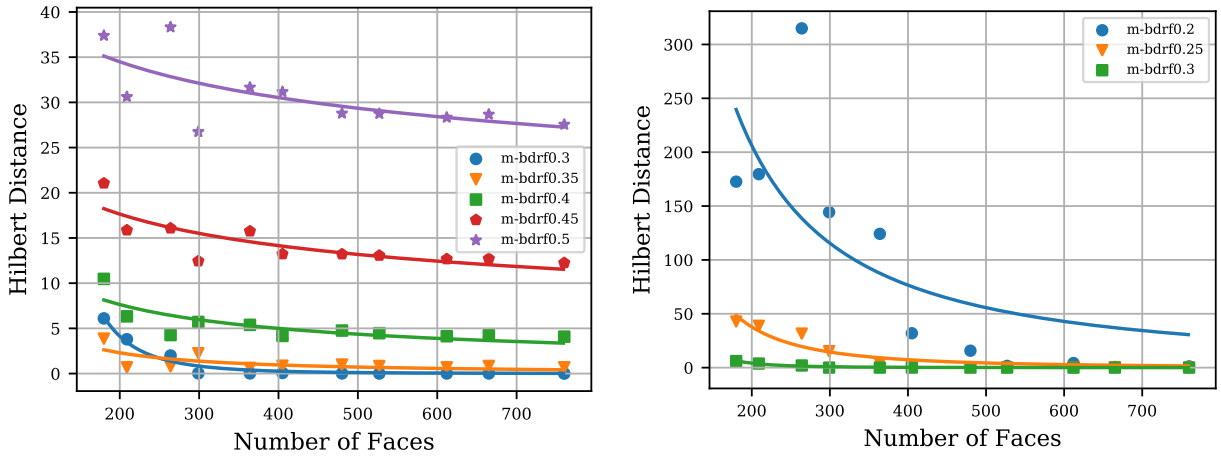

(a) Increasing m values.

(b) Decreasing m values.

Figure 6: Hilbert distance as a result of changes to the root mean slope term, m, measuring from $m = 0.3$.

Table 2: Table of model inputs.

Input Parameter	Value
Start Time	15:53:54 13/10/2014 UTC
Stop Time	15:57:47 13/10/2014 UTC
Duration	233 s
Observation Site Longitude	41.43 deg
Observation Site Latitude	41.43 deg
Observation Site Altitude	2030 m
Attitude	[0, 0, 0] $radians$
Attitude Motion	[0, 0, 0] $radians/s$
BDRF d	1.0
BDRF s	0.0

incidence, F_0, was taken as being equal to the diffuse albedo, ω. The specular component therefore not only depends on the RMS term m, which is non-negative and typically less than 0.5, but also on the diffuse albedo. However, the effects on the total specular reflection from changes in ω are negligible and so are ignored. With the reflection set to purely specular, m was varied from 0.05 - 0.5. Fig. 6 shows this result. On the left, distance is measured from the $m = 0.3$ case, as m is decreased. The right graph measures distance from $m = 0.3$, for an increasing value for m.

Next, the diffuse-to-specular ratio is tested. With the diffuse albedo, ω, set to 0.5 and the RMS slope term, m, set to 0.25, the diffuse and specular coefficients were varied from 0 - 1, maintaining the $s + d = 1$ condition. Attitude and attitude motion were set to zero. Fig. 7 plots this result with distance measured from the $d = 1.0$ case.

Fig. 8 repeats the initial attitude results of Fig 4, but now for a purely specular reflection. All other parameters are the same.

There is one final parameter to examine. To generate a light curve, the target object must be illuminated, and the observatory must be in darkness. Therefore, there are only certain times of day at which light curves are possible, defined by the location of the observatory. The following graph, in Fig. 9, repeats the purely diffuse and zero attitude case, but for a light curve acquired at a 10-hour offset. These inputs are presented in Table 2.

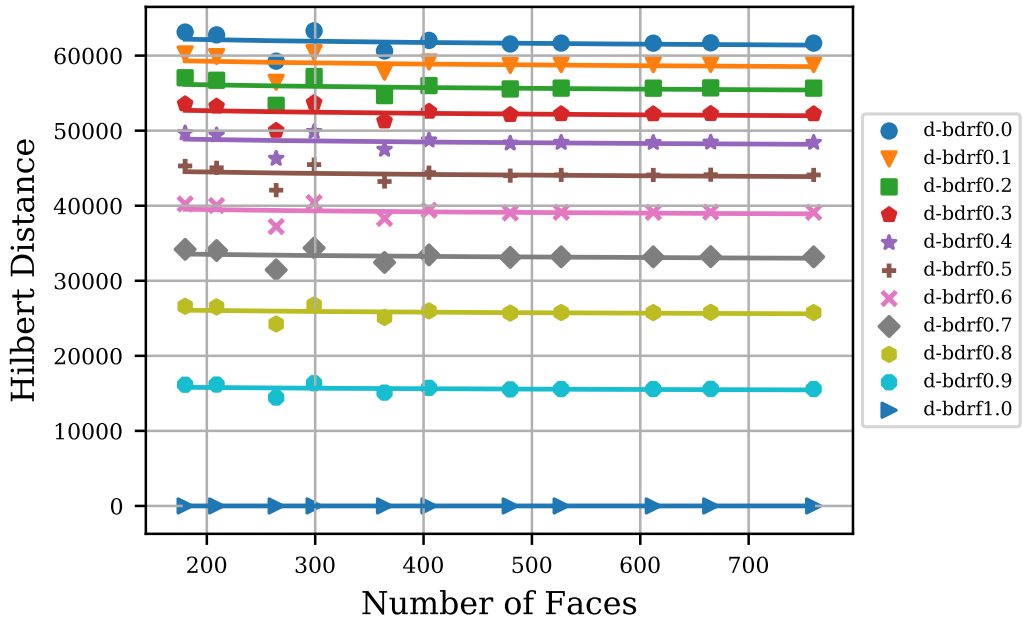

Figure 7: *The Hilbert distance resulting from an increase in the specular ratio with distance measured from the purely diffuse case, $d = 1.0$.*

4 Discussion

Firstly, Fig. 3 for changes in the diffuse albedo, ω, will be considered. The results shown on the left, which plots Hilbert distance for a decreasing ω, show an increasing distance from the base case. The results on the right, which plots Hilbert distance from an increasing ω, show a roughly uniform increase from the baseline for each successive increase in ω. Hence if the diffuse albedo is high, small changes in albedo will only cause small changes in the synthetic light curve. Alternatively, if the albedo is low, increasing the value produces a much larger change in the synthetic light curve, which increases uniformly for additional albedo increases. In both graphs, increases or decreases in diffuse albedo effect all data points equally, either shifting their values up or down. This behaviour is consistent across all facet numbers, which, relative to the diffuse albedo, have no effect.

The next four graphs in Fig. 4 present the results for a change in initial attitude for a purely diffuse reflection. In the frame in which the attitude is applied, the y-axis is aligned with the Earth radial vector. As a result, due to the initial conditions defined by the real light curve, the y-axis is closely aligned to the observation vector. Therefore an initial rotation in this axis should have a very minor effect on the synthetic light curve. This is reflected by Fig. 4b, where the maximum distance induced in the first data-point by any increase in the initial y-attitude is less than 0.05. By decreasing the number of facets, this distance is increased and the individual attitude cases begin to diverge. Similarities between the early and later attitude cases are a result of the symmetry in the geometry and an approach towards a π-radians rotation. The x-axis is aligned with the orbital velocity vector, so a rotation in this axis causes a change in illumination conditions. As a result, the distance increase for each attitude case is larger than for the y-axis. The maximum increase in distance in the first data-point as a result of a change in initial x-attitude is above 0.16. The more unusual behaviour caused by a decrease in number of facets is caused by the geometry pole, the point at which the vertices intersect, being orientated with the observer. This region of the geometry is particularly sensitive to changes in the number of facets. Finally, for the z-axis, distance increases due to an initial attitude are by far the largest, with a maximum of approximately 1.2 in the first data-point. The subsequent increases in distance due to a decreasing number of facets are also the largest. This is to be expected as rotations in the z-axis, which is coincident with the geometry pole, result in large changes in the reflection conditions. The final graph in Fig. 4 shows the result of adding the initial attitude equally into all three directions. The results of this graph are clearly dominated by the

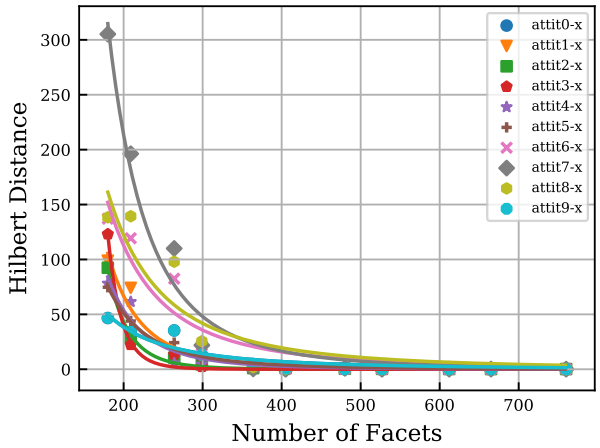

(a) Increasing initial x-attitude.

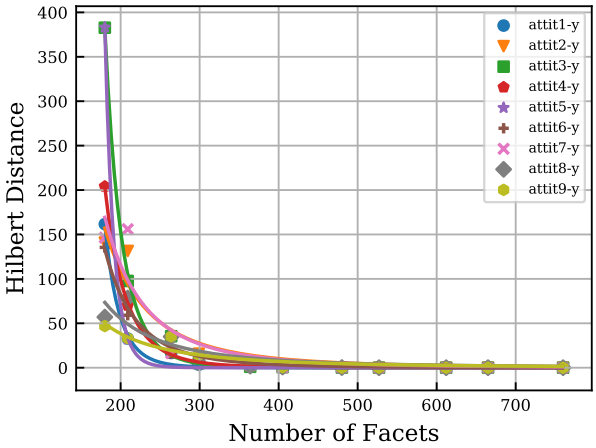

(b) Increasing initial y-attitude.

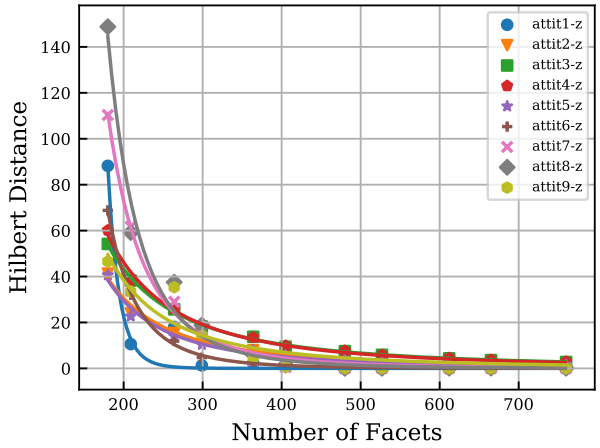

(c) Increasing initial z-attitude.

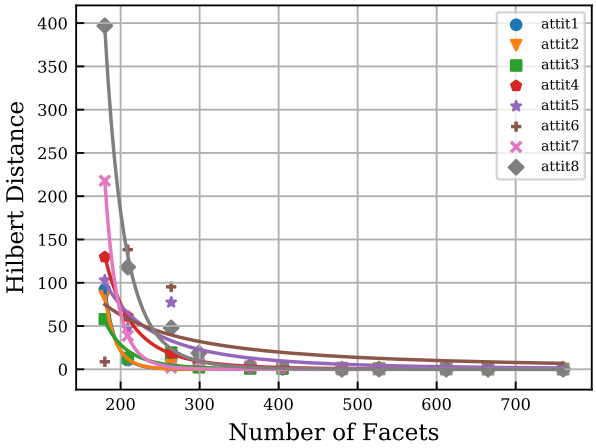

(d) Increasing initial attitude, equally into x, y and z.

Figure 8: With distance measured from the 760-facet zero-attitude case, the Hilbert distance resulting from changes in initial attitude for a purely specular reflection.

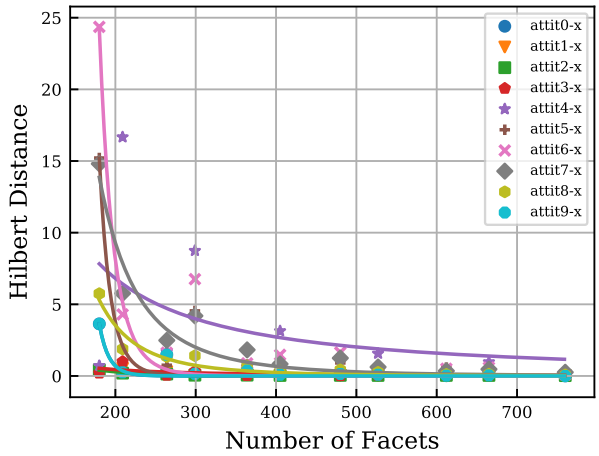

(a) Increasing initial x-attitude.

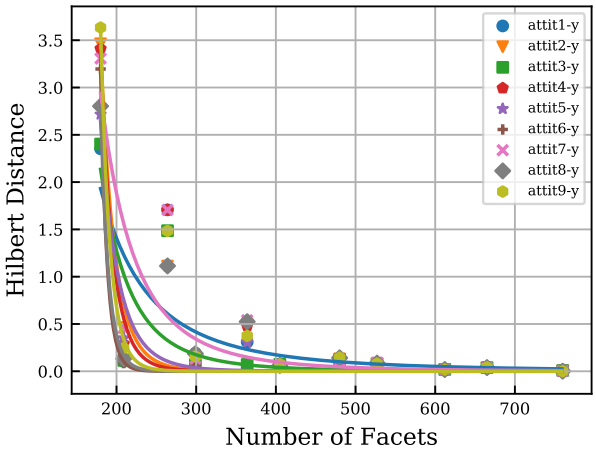

(b) Increasing initial y-attitude.

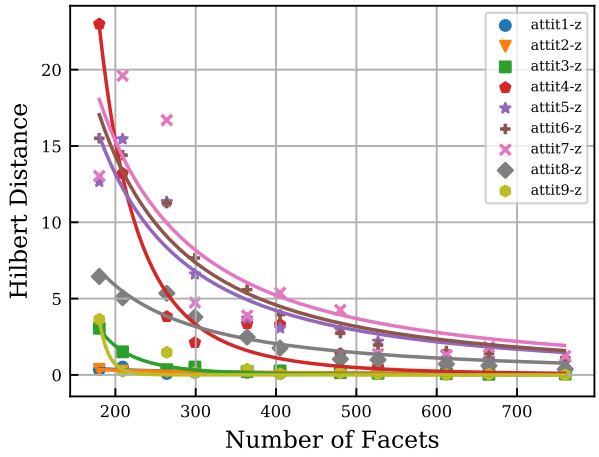

(c) Increasing initial z-attitude.

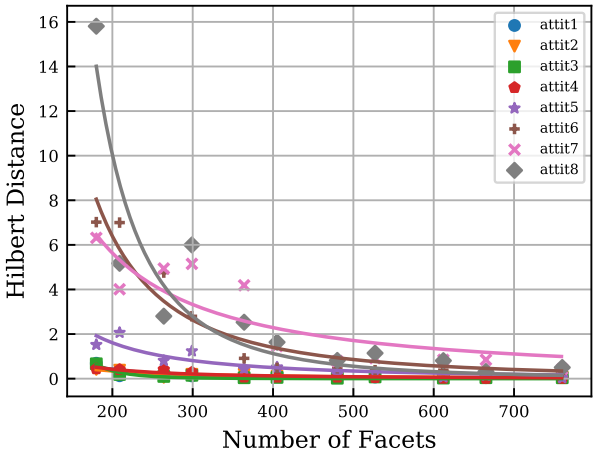

(d) Increasing initial attitude, equally into x, y and z.

Figure 9: The resulting Hilbert distance, measured from the 760-facet zero attitude case, for changes in initial attitude and a purely diffuse reflection.

z-axis rotation. In all four cases, the model was sensitive to the initial attitude state at high facet-numbers. However, as facet number is decreased, it quickly becomes the largest source of differences to the base case. Additionally, different initial attitudes result in differing responses due to decreasing facet numbers.

The attitude motion graphs in Fig. 5 exhibit a similar behaviour to the attitude cases. The z-axis rotation has the largest effect, and the y-axis the least. The behaviour is also similar as facet number is reduced. However, unlike the attitude cases, increases in attitude motion produce very small changes in the synthetic light curve. Although as facet number is reduced the cases begin to diverge, the differences remain much smaller than in the initial attitude cases. This is to be expected from a spherical geometry. As in the x-axis attitude case, the behaviour of x-axis attitude motion cases at lower facet numbers has been affected by the highly facet-sensitive geometry pole. The fourth graph plots the result of adding the attitude motion equally into all three axes. These results show that above 700 facets, the model is sensitive enough to discern different attitude motion rates of a sphere. Below 700, the number of facets becomes dominant.

The subsequent graphs examine the specular component of the model. The two graphs in Fig. 6 plot the results for changes in the RMS term, m, which parameterises the surface roughness. In each graph, distance is measured from the $m = 0.3$ base case. Considering the graph on the left, as m is increased beyond 0.3, an increasing distance is observed. This distance is further increased by reductions in facet numbers, with a larger effect for values further from the base case. This behaviour is repeated in the graph on the right for decreasing m, but with higher still variations for lower facet numbers. This is to be expected, as lower facet numbers lead to larger facet areas, and lower values for m indicate a smoother surface and hence a stronger specular reflection. The combination of these two effects causes large changes in the synthetic light curve.

The graph in Fig. 7 shows distance resulting from variations in the diffuse to specular ratio. The graph shows that a very large distance is caused by increasing the specular component, with the largest increase due to the initial introduction. For all the cases, decreasing facet numbers caused a further but far smaller distance increase. In general, increasing the specular component shifts all data-points up roughly equally, but increases magnitude of the variations at low facet numbers.

The four graphs in Fig. 8 repeat the attitude experiment for the purely specular case. At high facet numbers, the behaviour is similar to the diffuse case. The largest difference in the first data-point, approximately 3, is due to the z-axis, and the lowest, approximately 0.006, is due to the y-axis. However, the number of facets now causes distance increases orders of magnitude higher.

The final four graphs, Fig. 9, repeat the purely diffuse zero attitude case, but with a 10-hour offset in time. The result of this offset is a change in the initial observation and illumination angles. The graphs exhibit much of the same features as the first set of graphs. However, as a result of the observation axis no longer being closely aligned with the y-rotation axis, the behaviours of the first attitude case are spread across each axis. The effect of the geometry pole, which in the first case was confined to the x-axis, can now additionally be observed in the y-axis and to a lesser extent in the z-axis. Consequently the maximum distance produced from attitude offsets in the x and y-axes are larger than in the first case.

5 Conclusions

By far the largest changes to the synthetic light curve arise from the diffuse albedo and ratio of diffuse-to-specular reflection. Although differences in diffuse albedo result in large distances, it is a scaling parameter which affects all data-points equally and so does not factor into later results. The ratio of diffuse-to-specular reflection has an even larger effect, which further increases at lower facet numbers. This can be explained by the fewer, larger-area, facets with highly specular reflections causing a significant difference in the synthetic light curve.

In considering attitude, both the specular and diffuse operation of the model was examined. In both cases it was found that, at sufficiently high facet numbers, the model was sensitive to attitude and attitude motion. However, once decreased, number of facets quickly becomes the cause of the most significant differences. The results also show the specular reflections to have a much higher sensitivity to facet number than the diffuse reflection.

This paper has therefore shown that in synthetic light curve generation, accurately modelling object geometry and the specular and diffuse reflection characteristics are the most important considerations. Small inaccuracies in these parameters can result in large differences to the synthetic light curve. For the special case of a sphere, and assuming the diffuse and specular components are accurately modelled, a 760-facet spherical geometry exhibited a measurable attitude and attitude motion. This shows the model to be sensitive to subtly different attitude states.

The future work will pair this forward modelling with inverse modelling techniques for attitude determination.

References

[1] A Biryukov, G Beskin, S Karpov, S Bondar, E Ivanov, E Katkova, A Perkov, and V Sasyuk. The first light of Mini-MegaTORTORA wide-field monitoring system. 24:100–108, 2014. URL http://arxiv.org/abs/1411.2552.

[2] R.L. Cook and K.E. Torrance. A Reflectance Model for Computer Graphics. *ACM SIGGRAPH Computer Graphics*, 15(3):307–316, 1982. ISSN 00978930. doi: 10.1145/965161.806819.

[3] J. Goguen, J. Veverka, J. L. Elliot, and C. Church. The lightcurve and rotation period of asteroid 139 Juewa. *Icarus*, 29(1):137–142, 1976. ISSN 10902643. doi: 10.1016/0019-1035(76)90108-1.

[4] Joanna C Hinks, Richard Linares, and John L Crassidis. Attitude Observability from Light Curve Measurements. In *AIAA Guidance, Navigation, and Control (GNC) Conference*, pages 1–10, Boston, MA, 2013. ISBN 9781624102240. doi: 10.2514/6.2013-5005.

[5] M Kaasalainen, J Torppa, and K Muinonen. Optimization Methods for Asteroid Lightcurve Inversion II. The Complete Inverse Problem. *Icarus*, 153:37–51, 2001. ISSN 00191035. doi: 10.1006. URL http://www.idealibrary.com.

[6] N Koshkin, E Korobeynikova, L Shakun, S Strakhova, and Z H Tang. Remote Sensing of the EnviSat and Cbers-2B satellites rotation around the centre of mass by photometry. *Advances in Space Research*, 58(3):358–371, 2016. ISSN 18791948. doi: 10.1016/j.asr.2016.04.024. URL http://dx.doi.org/10.1016/j.asr.2016.04.024.

[7] Hugh G. Lewis, Graham G. Swinerd, Rebecca J. Newland, and Arrun Saunders. Active removal study for on-orbit debris using damage. *European Space Agency, (Special Publication) ESA SP*, 672 SP(April), 2009. ISSN 03796566.

[8] J. C. Liou and N. L. Johnson. Instability of the present LEO satellite populations. *Advances in Space Research*, 41(7):1046–1053, 2008. ISSN 02731177. doi: 10.1016/j.asr.2007.04.081.

[9] J. C. Liou and Nicholas L. Johnson. A sensitivity study of the effectiveness of active debris removal in LEO. *Acta Astronautica*, 64(2-3):236–243, 2009. ISSN 00945765. doi: 10.1016/j.actaastro.2008.07.009.

[10] David L Rabinowitz, K M Barkume, M E Brown, Henry Roe, Michael Schwartz, Suzanne Tourtellotte, and Chad Trujillo. Photometric Observations Constraining the Size, Shape, and Albedo of 2003 EL61, a Rapidly Rotating, Pluto-sized Object in the Kuiper Belt. *The Astrophysical Journal*, 639(2):1238–1251, 2006. ISSN 0004-637X. doi: 10.1086/499575. URL http://stacks.iop.org/0004-637X/639/i=2/a=1238{\%}5Cnpapers3://publication/doi/10.1086/499575.

[11] Karen Saxe. *Beginning Functional Analysis*. Springer-Verlag, New York, 1 edition, 2002. ISBN 978-1-4419-2914-3. doi: 10.1007/978-1-4757-3687-8.

[12] Charles J Wetterer and Moriba K Jah. Attitude Determination from Light Curves. *Journal of Guidance, Control, and Dynamics*, 32(5):1648–1651, 2009. ISSN 0731-5090. doi: 10.2514/1.44254. URL http://arc.aiaa.org/doi/abs/10.2514/1.44254.